

**A REFINED INTERACTION METHOD FOR DNS OF  
TRANSITION IN SEPARATED BOUNDARY LAYERS**

# A REFINED INTERACTION METHOD FOR DNS OF TRANSITION IN SEPARATED BOUNDARY LAYERS

Ulrich Maucher\*, Ulrich Rist†, and Siegfried Wagner‡  
*Institut für Aerodynamik und Gasdynamik, Universität Stuttgart,  
Pfaffenwaldring 21, 70550 Stuttgart, Germany*

## Abstract

In direct numerical simulations (DNS) of the transition in laminar separation bubbles the definition of a well-posed free-stream boundary condition is crucial. Different, partially contradicting properties are required: first of all, separation is forced by prescribing the streamwise velocity component. Moreover, oscillations occur at the free-stream boundary due to disturbance waves, which extend from the rapidly growing boundary layer far out into the potential flow. Finally, displacement effects of the separation bubble influence the surrounding potential flow by the so-called viscous-inviscid boundary-layer interaction. Usually, either the integration domain has to be sufficiently high or a state-of-the-art boundary layer interaction model based on the theory of thin airfoils can be applied. At high Reynolds number, neither of both possibilities is applicable. Therefore, an improved model for larger Reynolds numbers has been developed which meets the above mentioned requirements. The method is validated by variations of the height of the integration domain and by comparisons with experiments. It is shown, that even if the height of the integration domain covers only one boundary-layer thickness, the model works properly.

## Nomenclature

$c$	chord length,
$c_i$	blending function in interaction model,
$C_u, c_{u,ij}$	matrix and its coefficients, eqn. (14),(15),
$C_v, c_{v,ij}$	matrix and its coefficients, eqn. (11),(12),
$f_c$	polynomial function (interaction model),
$H_{12}$	shape parameter,
$I$	total number of discrete sources in the model,
$L$	reference length,
$Ma$	Mach number,
$n_1, n_2, \Delta n$	number of first and last $x$ -station and $x$ -increment of the source distribution in the model, respectively,
$p_w$	pressure at the wall,
$Re$	Reynolds number,

---

\*Research Assistant, Member AIAA

†Research Scientist

‡Professor, Aero- and Gasdynamics, Member AIAA

$Re_{\delta_1}$	Reynolds number based on displacement thickness,
$q$	source distribution in the interaction model,
$t$	time,
$T_{TS}$	forcing cycle of the TS wave,
$u, v, w$	velocity components in $x$ , $y$ , and $z$ -direction, respectively,
$U_2$	first higher harmonic of TS-wave,
$u_\infty$	reference velocity,
$x, y, z$	streamwise, wall-normal, and spanwise coordinate, respectively,
$x_{ia}$	begin of instantaneous update in interaction model,
$\alpha$	streamwise wave number: $\alpha = 2\pi/\lambda_x$ ,
$\alpha_e$	assumed streamwise wavenumber at free stream boundary,
$\alpha^*$	assumed total wavenumber at free stream boundary,
$\gamma$	spanwise wave number: $\gamma = 2\pi/\lambda_z$ ,
$\tilde{\Delta}$	modified Laplace operator, eqn. (3),
$\delta_1$	displacement thickness: $\int_0^{y_e} (1 - \frac{u}{u_e}) dy$ ,
$\delta_2$	momentum thickness: $\int_0^{y_e} \frac{u}{u_e} (1 - \frac{u}{u_e}) dy$ ,
$\varepsilon_{ia}, \varepsilon_{inst}$	amplitude limits in interaction model,
$\xi_{ij}$	streamwise distance to a discrete source,
$\omega$	vorticity.

Subscripts, superscripts:

$e$	at free-stream boundary,
$i$	$x$ -station of induced velocity,
$j$	$x$ -station of inducing source,
$k$	spanwise spectral mode,
$p$	potential flow,
$s$	at separation,
$v$	due to viscosity,
<i>Capital</i>	Fourier transformed variable,
$I$	inverse matrix,
$-$	time-averaged variable,
$\wedge$	dimensional variable,
$\rightarrow$	vector.

## 1 Introduction

A boundary layer subject to a strong adverse pressure gradient is susceptible to separation. In the separated region, disturbance waves, so-called Tollmien-Schlichting (TS-) waves, are strongly amplified and transition to turbulence takes place. The increased dissipation causes momentum transfer towards the wall and finally forces the boundary layer to re-attach. Beside this more general understanding, the physics of laminar separation bubbles (LSB) is still not well understood. Apart from the acceleration of transition and the

according higher skin friction, laminar separation bubbles have strong impact on the aerodynamic properties of airfoils through the interaction of the boundary layer and the surrounding potential flow, the viscous-inviscid interaction. Displacement effects of the boundary layer can change the potential flow in the separated region or even worse, around the entire airfoil. A typical pressure plateau is generated near the separated region followed by a sudden pressure increase at the end of the bubble.

As the computers became more powerful, DNS turned out to be a well suited tool to investigate the physics of laminar separation bubbles. On the one hand, DNS can achieve very low (numerical) turbulence to investigate the self-excited behavior of separation bubbles (Gruber [1, 2], Pauley *et al.* [3], Lin & Pauley [4], Ripley & Pauley [5]). On the other hand, the interaction of special 2D and 3D disturbances is investigated in controlled “numerical experiments”. Rist [6] and Rist *et al.* [7, 8] were the first to perform controlled 3D simulations of the transition in a laminar separation bubble. They continued the work of Gruber which was restricted to 2D. By decelerating a Blasius boundary layer to  $\approx 91\%$  of the initial velocity Rist *et al.* forced the boundary layer to separate and a separation bubble to form. The Reynolds number based on displacement thickness at separation in these simulations was close to  $Re_{\delta_{1,s}} = 1250$ . Rist *et al.* forced different combinations of 2D and 3D waves upstream of the separation bubble and obtained a strictly convective behavior of all disturbance waves in the investigated test cases. They observe that secondary disturbance amplification breaks down as the amplitude of the 2D TS-wave saturates and transition to turbulence seems to be not due to secondary instability. Since weakly oblique 3D modes are almost as amplified as clean 2D waves they suggest that an Oblique Breakdown mechanism is very likely to occur and to provide the three-dimensionality needed for transition to turbulence. If the Reynolds number is further increased to  $Re_{\delta_{1,s}} = 2400$ , Maucher *et al.* [9] found temporal growth of 3D modes, with the presence of a saturated 2D TS-wave (amplitude  $\approx 20\% u_\infty$ ) in the re-attachment region. This temporal growth increases if the separation bubble is bigger especially in terms of the reverse flow intensity. It finally causes transition to turbulence even if the flow is purely 2D upstream of the separation bubble (Maucher *et al.* [10]).

Wasistho [11], Alam & Sandham [12], and Spalart & Strelets [13] performed DNS focusing on the development of turbulence downstream of the LSB including, however, the whole separation bubble in the integration domain. The Reynolds number in those investigations is  $Re_{\delta_{1,s}} \lesssim 1000$ . Wasistho uses a compressible numerical code at  $Ma = 0.2$  and forces a 2D TS-wave and a pair of 3D waves with an amplitude of 1 percent  $u_\infty$ , each. From the observation of a three-dimensionally deformed wave front in terms of spanwise vorticity, which he denotes as  $\Lambda$ -shaped, he concludes that  $\Lambda$ -vortices are present. Alam & Sandham [12, 14] force a pair of symmetrically oblique waves with large amplitude. In their simulation transition is characterized by a staggered pattern of  $\Lambda$ -vortices which might be due to a by-pass mechanism. Spalart & Strelets [13] use a spectral ansatz in streamwise direction. Disturbances propagating into the fringe-region are damped to moder-

ate amplitudes and feed arbitrary 2D and 3D disturbances with amplitudes about  $5 \times 10^{-4}$  into the Blasius boundary layer upstream of separation. They observe a flapping of the free shear-layer in the front part of the separation bubble which dominates by far in comparison with convective disturbance waves. Whether the flapping or possible large amplitude traveling waves cause transition remains unclear.

## 1.1 Free-stream boundary-conditions

There are, in general, two approaches to decelerate the boundary layer and thus force separation. The first approach prescribes a wall-normal velocity distribution  $v_e$  at the free-stream boundary of the integration domain. This is similar to an experimental apparatus, where transition at a flat plate is forced by a displacement body or by suction through the opposite wall in a channel (here denoted as channel formulation). This method is used by the most of the above mentioned authors. In the second approach, in contrast, basing on the work of Gruber and Rist we prescribe the streamwise velocity component at the free stream  $u_e$  and allow for displacement effects by applying a von-Neumann boundary condition for the wall-normal velocity component which is defined according to the equation of continuity ( $\frac{\partial v}{\partial y}|_e = -\frac{du_e}{dx}$ ;  $x$  and  $y$  are the streamwise and wall-normal coordinates, respectively). This procedure is strongly related to boundary-layer methods and meets the conditions at an airfoil, where a decelerated velocity distribution is forced upon the boundary layer by the inviscid streamwise velocity distribution and where no walls limit displacement in the far-away flow field (termed free-flight formulation further down).

Wasistho *et al.* [15] prescribe the wall normal distribution obtained in a first simulation with a fixed streamwise  $u_e$  distribution (case A) as wall-normal boundary condition in a second DNS (case B). They prove that the results of both DNS (A and B) are equivalent.

Hsiao & Pauley [16] compare results for marginal separation at low Reynolds number obtained by DNS (channel formulation) and with a boundary layer approach, where the viscous-inviscid boundary layer interaction was taken into account (free-flight formulation). In the DNS a suction port with a fixed suction distribution was inserted into an elsewhere non-transpiration free-stream boundary. Even in a very high integration domain separation was strongly delayed in DNS by the displacement of the growing boundary layer which accelerates the flow in comparison with the boundary layer method due to a narrowing of the “channel”. When the non-transpiration condition is replaced by a von-Neumann condition for the wall-normal velocity component outside the suction port Hsiao & Pauley gained favorable agreement with the boundary layer method (modification towards free-flight condition). On the other hand this limits the width of the suction port to small streamwise extends.

Spalart & Strelets [13] apply a suction port according to the original boundary condition of Hsiao & Pauley. The flapping of the free shear-layer in their DNS might be caused by “channel”-effects, a strong unsteady widening

and narrowing of the effective channel height due to unsteady displacement effects. If one imagines an experiment in a very low channel with a height of only a few boundary-layer thicknesses, according to typical boxes in DNS, it is evident that blockage effects may have strong impact on the streamwise potential velocity component and thus on the pressure distribution, especially if an unsteady separation bubble appears.

Hildings [17] recalculates an experiment, where separation was forced on a flat plate by a displacement body at the opposing wind-tunnel wall. He prescribes either the measured wall-normal (channel formulation) or streamwise velocity component at the free-stream (free-flight formulation) and calculates the respective missing component according to the condition of vanishing spanwise vorticity at the free-stream ( $\frac{\partial u}{\partial y}|_e = \frac{\partial v}{\partial x}|_e$ ). Thus, in the free-flight formulation a Dirichlet boundary-condition is applied for the wall-normal velocity component. Both formulations achieve only coarse qualitative agreement with the experimental findings. The channel formulation cannot guarantee to accurately reproduce the flow in an experimental channel, since usually the computational box is low in comparison with the height of the channel. In our institute, Müller began promising attempts to reproduce the same experiment with our boundary condition (free-flight formulation, von-Neumann condition for  $v$ ). If the computational box does not cover the whole channel height, a channel resembles properties inherent in both formulations, the channel formulation and the free-flight formulation. Nevertheless, there are first hints that even here the free-flight formulation is superior if the computational box covers only a smaller part of the experimental channel. However, for reliable statements further research is necessary.

Our calculations (with the free-flight formulation) of airfoil separation bubbles show, that the velocity distribution at the edge of the boundary layer deviates from the prescribed distribution at the free stream boundary (see later in this paper). A typical velocity distribution with a velocity plateau appears, even if the integration domain covers only a few heights of the boundary layer, since a relaxation of the potential velocity towards the free-stream boundary takes place. Actually, this formulation captures the main properties of LSB on airfoils. The definition of an appropriate boundary condition with the channel formulation, in contrast, is very difficult. The final wall-normal velocity distribution at the airfoil is not known at the beginning of the DNS, and the definition of the boundary condition needs to make assumptions, which in turn have strong impact on the development of the LSB. Prescribing the wall-normal component at the free-stream in DNS of airfoil separation-bubbles therefore requires a detailed knowledge about the effects of the LSB, whereas prescribing the streamwise component primary rests on the usually a priori known inviscid velocity distribution which finally causes separation. Besides these general differences, the findings of Hsiao & Pauley as well as our experience are evidence of the advantages of a von-Neumann condition for the wall-normal velocity component in DNS of airfoil LSB.

At high Reynolds numbers ( $Re_{\delta_1} \approx 2000$ ) none of the mentioned approaches yields satisfactory solutions for LSB on airfoils. To obtain quan-

titative findings the effect of boundary layer interaction at the free-stream boundary may not be neglected. This problem is addressed in the present paper.

Since the seventies strong attempts to model the boundary-layer interaction in numerical schemes were made. Now, “viscous-inviscid boundary-layer interaction models” are frequently used for boundary layer calculations in flat integration domains, where the wall-normal extent is very small compared with the streamwise extent. In such models the initially prescribed (inviscid) potential velocity distribution  $u_p$  is superposed with a viscous component (index  $v$ ) due to the displacement of the boundary layer. The displacement is regarded as a modification of the shape of the wall contour and is modeled with a distribution of sources and sinks  $q(x)$  at the wall. The velocity distribution  $u_p$  is updated by adding the streamwise velocity component  $u_v$  which is induced by the sources at the wall. Employing the theory of thin airfoils [18], the sources can be easily calculated (Veldman [19]):

$$v_v(x) = \frac{d}{dx}(u_p \delta_1), \quad q(x) = \frac{1}{2}v_v(x), \quad (1)$$

where  $\delta_1$  denotes the displacement thickness.

Gruber [2] applied such a model to his DNS code for the investigation of 2D instability in laminar separation bubbles. He shows that the wall-normal viscous velocity-component  $v_v$  at the free-stream boundary is connected to the instantaneous wall-normal value  $v(x, y = y_e)$  and an inviscid part  $v_p$ :

$$v_v(x) = v(x, y_e) - \int_0^{y_e} \frac{\partial v_p}{\partial y} dy = v(x, y_e) + y_e \frac{du_p}{dx}. \quad (2)$$

He tested this method at small Reynolds numbers ( $Re_{\delta_{1,s}} \approx 600$ ) and obtained reliable results.

Tests with Gruber’s model at Reynolds numbers typical for mid-chord bubbles of glider wing-sections or high-lift devices ( $Re_{\delta_{1,s}} \approx 2500$ ) failed. At best, only coarse qualitative agreement with the experiment can be obtained. Such simulations demand a tall integration domain and the theory of thin airfoils increasingly overestimates the streamwise viscous component  $u_v$  in higher integration domains. Moreover, disturbance waves extend far out into the potential flow and cause oscillations at the upper boundary which, in consequence, are modeled as source distribution at the wall. Errors due to the simplifications in the model (i.e., the displacement is modeled at the wall and not in the boundary layer, where it originates) decay only slowly in streamwise direction ( $\propto 1/x$ ) compared to TS-waves, which might be generated far upstream of the bubble by such errors. If once generated, they are amplified exponentially to such amplitudes which can exceed the amplitude of the initiating errors in the separated region by far, rendering the DNS useless.

Nevertheless, in DNS of LSB at high Reynolds numbers there are numerical motivations for the application of an interaction model. Imposing the velocity distribution in a low domain has a very rigid impact on the velocity distribution at the edge of the boundary layer. Displacement effects

are mostly suppressed. Very high domains allow for changes of the potential flow in wall-normal direction. The velocity at the edge of the boundary layer thus differs from the prescribed potential velocity distribution at the upper boundary of the integration domain. If the height of the integration domain is varied, the edge-velocity distribution therefore changes in spite of similar boundary conditions. A well-defined interaction model has to capture the displacement effects properly, simultaneously avoiding the dependency on the height of the integration domain.

## 2 Numerical Method

### 2.1 Governing equations

The DNS numerical scheme is based on the complete incompressible Navier-Stokes equations in vorticity-transport formulation [20, 21]

$$\begin{aligned}\frac{\partial \omega_x}{\partial t} + \frac{\partial}{\partial y}(v\omega_x - u\omega_y) + \frac{\partial}{\partial z}(w\omega_x - u\omega_z) &= \tilde{\Delta} \omega_x, \\ \frac{\partial \omega_y}{\partial t} + \frac{\partial}{\partial x}(u\omega_y - v\omega_x) + \frac{\partial}{\partial z}(w\omega_y - v\omega_z) &= \tilde{\Delta} \omega_y, \\ \frac{\partial \omega_z}{\partial t} + \frac{\partial}{\partial x}(u\omega_z - w\omega_x) + \frac{\partial}{\partial y}(v\omega_z - w\omega_y) &= \tilde{\Delta} \omega_z,\end{aligned}$$

with  $\tilde{\Delta} = \frac{1}{Re} \frac{\partial^2}{\partial x^2} + \frac{\partial^2}{\partial y^2} + \frac{1}{Re} \frac{\partial^2}{\partial z^2}$  (3)

which are solved in a rectangular integration domain (figure 1).  $\omega$  denotes the vorticity.  $u, v, w$  are the velocity components in streamwise ( $x$ ), wall-normal ( $y$ ), and spanwise ( $z$ ) direction, respectively. All variables are non-dimensionalized by a reference length  $\hat{L}$ , by the velocity  $\hat{U}_\infty$ , and the Reynolds number  $Re = \hat{u}_\infty \hat{L} / \hat{\nu}$ , where  $\hat{\cdot}$  denotes dimensional variables and  $\hat{\nu}$  is the kinematic viscosity:

$$\begin{aligned}x &= \frac{\hat{x}}{\hat{L}}, \quad y = \sqrt{Re} \frac{\hat{y}}{\hat{L}}, \quad z = \frac{\hat{z}}{\hat{L}}, \\ u &= \frac{\hat{u}}{\hat{u}_\infty}, \quad v = \sqrt{Re} \frac{\hat{v}}{\hat{u}_\infty}, \quad w = \frac{\hat{w}}{\hat{u}_\infty}.\end{aligned} \tag{4}$$

Additionally, the variables in wall-normal direction  $y$  and  $v$  are stretched by  $\sqrt{Re}$ . This leads to the definition of the non-dimensionalized vorticity components:

$$\begin{aligned}\omega_x &= \frac{1}{Re} \frac{\partial v}{\partial z} - \frac{\partial w}{\partial y}, \\ \omega_y &= -\frac{\partial u}{\partial z} + \frac{\partial w}{\partial x}, \\ \omega_z &= \frac{\partial u}{\partial y} - \frac{1}{Re} \frac{\partial v}{\partial x}.\end{aligned} \tag{5}$$

The velocity components can be computed from three Poisson equations:

$$\frac{\partial^2 u}{\partial x^2} + \frac{\partial^2 u}{\partial z^2} = -\frac{\partial \omega_y}{\partial z} - \frac{\partial^2 v}{\partial x \partial y}, \quad (6)$$

$$\tilde{\Delta} v = \frac{\partial \omega_x}{\partial z} - \frac{\partial \omega_z}{\partial x}, \quad (7)$$

$$\frac{\partial^2 w}{\partial x^2} + \frac{\partial^2 w}{\partial z^2} = \frac{\partial \omega_y}{\partial x} - \frac{\partial^2 v}{\partial y \partial z}. \quad (8)$$

## 2.2 Boundary conditions and discretization

In *spanwise direction* a spectral ansatz is applied which implies periodic boundary conditions. The equations are solved with a highly efficient, parallelized finite difference method, 4th order accurate in time (Runge-Kutta) and space. Due to the spectral ansatz in spanwise direction the  $u$  and  $w$  Poisson-equations (6, 8) can be solved independently for each spanwise spectral mode. They reduce to ODEs in streamwise direction and lead to penta-diagonal systems. Only the  $v$ -equation (7) has to be solved iteratively by a line relaxation method accelerated by a multigrid algorithm. The spectral ansatz allows to specify different boundary conditions for the 2D and 3D part of the flow.

Since the *free-stream boundary* is in the potential flow, all vorticity components vanish and are set to zero. The inviscid streamwise velocity component  $u_p$  is prescribed for the 2D part. With the continuity equation

$$\frac{\partial v_p}{\partial y} = -\frac{\partial u_p}{\partial x} \quad (9)$$

a 2D von-Neumann condition for  $v$  is defined. It allows for a wall-normal velocity component due to displacement effects even if no interaction model is applied. For the 3D part, exponential decay of the wall-normal velocity is assumed

$$\frac{\partial v_{3D}}{\partial y} = -\frac{\alpha_k^*}{\sqrt{Re}} v_{3D}, \quad (10)$$

where  $\alpha_k^* = \sqrt{\alpha_e^2 + (\gamma_k)^2}$  denotes an individual wavenumber specified for each spectral mode  $k$  which consists of the respective spanwise wavenumber  $\gamma_k$  and a streamwise wave-number  $\alpha_e$  which is considered to be representative for the whole streamwise extent of the integration domain (Fasel *et al.* [22]). In the potential flow, this condition is consistent with the exact solution for linear TS-waves with the streamwise wave number  $\alpha_e$ . In the progress of a rapid breakdown into fine length scales downstream of the separation bubble, small vortices are injected into the previously undisturbed potential flow. A buffer domain at the free-stream boundary damps the wall-normal derivatives of the vorticity-transport equations to zero when the vortices approach the free stream boundary and finally their wall-normal propagation is stopped. The assumption of inviscid flow at the very boundary remains valid.

At the *inflow boundary*, steady Falkner-Skan profiles, usually Blasius profiles are prescribed. The 3D part of the flow is set to zero. If controlled conditions are required, disturbance waves can be forced by periodic or pulse-like

wall-normal suction and blowing in a disturbance strip at the *wall*. Except for the disturbance strip, the no-slip condition is applied at the *wall*.

The unsteady vorticity components are smoothly damped to steady-state values in the relaminarization zone upstream of the *outflow boundary* [21]. Consequently, the unsteady velocity components also decay exponentially in streamwise direction and vanish at the outflow.

### 2.3 Boundary-layer interaction-model

To meet the requirements on the interaction model in DNS of separation bubbles at higher Reynolds numbers, the inviscid theory has to be applied without such assumptions as they are made in the theory of thin airfoils. The viscous component  $\vec{v}_{v,i}$  is modeled at each  $\Delta n$ -th of the total of  $N$  streamwise grid points in the limits from  $n_1$  near the inflow boundary to  $n_2$  upstream of the buffer domain at the outflow boundary, resulting in  $I = 1 + (n_2 - n_1)/\Delta n$  discrete sources  $\vec{q}_j$ :

$$\vec{v}_{v,i} = C_v \vec{q}_j. \quad (11)$$

The indices  $i$  and  $j$  denote the streamwise positions of the viscous velocity component  $v_v(x_i)$  and of the source  $q(x_j)$ , respectively, where  $1 \leq i, j \leq I$ . The matrix  $C_v$  has the coefficients

$$c_{v,ij} = \frac{1}{2\pi} \frac{y_e}{\xi_{ij}^2 + y_e^2}, \quad (12)$$

where  $\xi_{ij}$  denotes the streamwise distance from the source ( $x_i - x_j$ ).  $C_v$  is inverted once at the beginning of the DNS, giving the relation

$$\vec{q}_j = C_v^I \vec{v}_{v,i}. \quad (13)$$

Since the matrix  $C_v$  is ill conditioned especially in high integration domains and for narrow spacing of the sources, a minimum spacing considerably larger than the streamwise discretization is required ( $\Delta n > 1$ ), at the same time limiting the total number  $I$  of sources used. Finally, the streamwise viscous velocity component is calculated at all  $x$ -stations between  $n_1$  and  $n_2$  from

$$\vec{u}_{v,n} = C_u \vec{q}_j, \quad (14)$$

where the  $(n_2 - n_1 + 1) \times I$  matrix  $C_u$  has the constant coefficients

$$c_{u,nj} = \frac{1}{2\pi} \frac{\xi_{nj}}{\xi_{nj}^2 + y_e^2}. \quad (15)$$

The boundary-layer interaction model is implemented into the multigrid scheme for solving the 2D part of the  $v$ -Poisson equation. The boundary conditions of the 3D spanwise spectral modes are not effected. During each multigrid cycle of the 2D  $v$ -Poisson equation (V-cycle with 4 grids and 2/10/1 iterations on the respective grid after coarsening/ on the coarsest grid/ after refinement), the von-Neumann condition at the free-stream boundary is fixed. At the end of the cycle equations (2), (13), and (14) are calculated to update

the von-Neumann condition at the free-stream boundary of the  $v$ -Poisson equation

$$\left. \frac{\partial v}{\partial y} \right|_e = -\frac{d(u_v + u_p)}{dx}. \quad (16)$$

It turned out that  $u_v$  should be adapted with an under-relaxation of 0.55 for optimum convergence. This procedure is only repeated for the first three of a total of eight multigrid-cycles. On the one hand, since the variation of  $u_v$  stops decaying from one cycle to the next. On the other hand, the convergence of the multigrid scheme is much worse when the model is active than without it.

The instantaneous update of the viscous component is very efficient at streamwise stations where the free-stream disturbance amplitude is still large compared to the maximum in the boundary layer. In particular, downstream of the LSB even high-frequency displacement effects caused by large amplitude vortices are captured, and an accurate treatment of such oscillations at the free-stream boundary is ensured (see next section). In turn, strong detrimental upstream influence might be caused by such oscillations. This is probably the main source of errors in the model. According to the linear stability theory (LST), TS-waves do not cause displacement because the displacement due to the near-wall maximum is compensated by the reverse effect of the 2nd maximum in the  $u$ -eigenfunction. The wall-normal velocity component vanishes with increasing distance from the wall and finally approaches zero. In contrast, the model takes into account only the displacement up to the location of the free-stream boundary and omits the rest. Thus, in the model, each TS-wave has a significant displacement effect. The respective sources and sinks induce oscillations at the entire free-stream boundary. However, the mean value of those oscillations is low (for a linear TS-wave it is zero).

In order to suppress the above mentioned errors (oscillations), the region upstream of the separation bubble is treated in a special manner. It is sufficient to just model the time-averaged displacement effects at streamwise stations where the TS-amplitude at the free-stream boundary is small compared to the amplitude in the boundary layer. At the same time it is crucial to suppress oscillations which are generated by large amplitude vortices further downstream. Therefore, the mean  $\bar{u}_v(x)$  and the Fourier-amplitude  $U_v$  of the instantaneously induced streamwise velocity component  $u_v(x, t)$  (where  $t$  denotes the time) are checked during each TS-period. Upstream of a position  $x_{ia}(t)$ , where the amplitude  $U_v(x)$  is below a limit of  $\varepsilon_{ia} = 2 \times 10^{-4}$  (figure 2a),  $u_v(x, t)$  is described by a polynomial function, valid for one TS-period:

$$f_c(x, t) = f_{c0}(x) + f_{c1}(x)t + f_{c2}(x)t^2 + f_{c3}(x)t^3 \quad (17)$$

to obtain a smooth temporal behavior. The coefficients  $f_{c0}(x)$ ,  $f_{c1}(x)$ ,  $f_{c2}(x)$ ,  $f_{c3}(x)$  are adjusted at the beginning of the respective TS-period ( $t = t_0$ ) in such a way, that  $f_c(x, t)$  is continuous up to its second time derivative, which results in three conditions for the evaluation of the four coefficients. For the required fourth condition assumptions for the end of the TS-Period

( $t = t_1 = t_0 + T_{TS}$ ) have to be made: either about the unknown function value  $f_c(x, t_1)$  or one of the time derivatives. Here, a combination of both is applied. The deviation  $f$  of the polynomial  $f_c(x, t)$  from a assumed target value  $f_t(x)$  and the first time derivative  $f'$  and second time derivative  $f''$  at the end of TS-Period ( $t = t_1$ ) are weighted in a special way:

$$\frac{3}{T_{TS}} \underbrace{[f_c(x, t_1) - f_t(x)]}_f + 3 \underbrace{\frac{\partial}{\partial t} f_c(x, t_1)}_{f'} + T_{TS} \underbrace{\frac{\partial^2}{\partial t^2} f_c(x, t_1)}_{f''} = 0. \quad (18)$$

Inserting equation (17) and re-arranging yields the missing fourth condition. If the target value (for example  $\bar{u}_v$ ) is constant, the weighting guarantees that the target value is gained by the polynomial function the latest after three TS-periods. However, in some DNS (with very small forcing amplitudes) even the changes of  $\bar{u}_v(x)$  from one TS-period to the next are too large compared with the TS-amplitude, and prescribing  $\bar{u}_v(x)$  as target value  $f_t(x)$  causes the excitation of disturbance waves upstream of the separation bubble. Nevertheless, those changes may be small enough not to affect the instability properties of the mean flow. Then, their cancellation is desired and has no influence on the amplification of TS-waves. A limit  $\varepsilon_{inst}$  is introduced, which marks the tolerable range for  $u_v(x)$  with negligible influence on the instability properties of the mean flow. If  $\bar{u}_v(x)$  is fitted in the limits of  $\pm\varepsilon_{inst}$  the disturbance amplification is not affected. A relaxation factor  $R_{ia}$  is defined, which depends on the difference between the mean in the past TS-period  $\bar{u}_v(x)$  and the instantaneous value of the polynomial function  $f_c(x, t_0)$ :

$$|\bar{u}_v(x) - f_c(x, t_0)| \begin{cases} \geq \varepsilon_{inst} & : R_{ia}(x) = 1 \\ < \varepsilon_{inst} & : R_{ia}(x) = \left( \frac{|\bar{u}_v(x) - f_c(x, t_0)|}{\varepsilon_{inst}} \right)^{1.5} \end{cases}. \quad (19)$$

The target value is calculated

$$f_t(x) = f_c(x, t_0) - R_{ia}(x) [f_c(x, t_0) - \bar{u}_v(x)] \quad (20)$$

and introduced into equation (18). The exponent causes a rapid decay of the relaxation factor  $R_{ia}$  towards zero, if  $|\bar{u}_v(x) - f_c(x, t_0)| < \varepsilon_{inst}$ . Thus  $f_c(x)$  becomes almost steady. In model calculations the properties of the ansatz are investigated. Its convergence properties are demonstrated by prescribing three initial conditions for  $f_c(t = 0)$  in figure 2b. The tolerable range  $\varepsilon_{inst}$  is assumed to be  $\pm 0.05$  (error bars), the mean is independent from time:  $\bar{u}_v(t) = 1$ . For all initial values of the function  $f_c(t = 0) = 0$  (solid line),  $f_c(t = 0) = 0.5$  (dashed line), or  $f_c(t = 0) = 0.95$  (dash-dotted line),  $f_c(t)$  approximates the desired range  $\pm\varepsilon_{inst}$  rapidly (error bars). If the updates of the coefficients are performed without relaxation ( $f_c$  outside the range  $\pm\varepsilon_{inst}$ )  $\bar{u}_v$  is gained exactly (solid line at  $t = 4T_{TS}$ ). With the initial value  $f_c(t = 0) = 0.5$  (dashed line) the update of the coefficients at  $t = 3T_{TS}$  is performed with an under-relaxation since  $f_c(t)$  already has entered the range of  $\bar{u}_v \pm \varepsilon_{inst}$ . The function  $f_c$  fails to gain  $\bar{u}_v = 1$  but becomes almost steady and is well inside the required range  $\varepsilon_{inst}$ . Of course, for initial values of  $f_c$

inside the range  $\pm\varepsilon_{inst}$  the same behaviour is observed (dash-dotted line). The curves in figure 2c address the damping of a harmonic oscillation of the mean  $\bar{u}_v$  with an amplitude  $A_{mean} = 0.5$  (circles). The development of the function  $f_c$  is investigated for three values of  $\varepsilon_{inst}$ . In the case of the solid line the limit  $\varepsilon_{inst}$  is set to be  $\varepsilon_{inst} = A_{mean} = 0.5$ . Actually, this agrees with the temporal behaviour of  $f_c$  when no relaxation is applied. The dashed line  $\varepsilon_{inst} = 2A_{mean} = 1$  marks moderate under-relaxation and the amplitude of the oscillation of  $f_c$  is reduced to one third in comparison with the case without relaxation. For  $\varepsilon_{inst} = 10A_{mean} = 5$  (dash-dotted line) the oscillation of the mean  $\bar{u}_v$  is strongly damped. The sub-figures prove, that on the one hand the required accuracy  $\bar{u}_v \pm \varepsilon_{inst}$  is gained rapidly (figure 2b), and on the other hand low amplitude oscillations are effectively damped (figure 2c). An appropriate value for  $\varepsilon_{inst}$  is 0.004 which ensures that the mean-velocity distribution is accurate enough to meet the required stability properties.

Downstream of  $x_{ia}$  the polynomial  $f_c(x, t)$  and the instantaneous values  $u_v(x, t)$  are weighted by means of a blending function  $c_i(x)$ , which is continuous up to the second derivative and changes from zero for  $x < x_{ia}$  to one for  $x > (x_{ia} + \Delta x_{ia})$ :

$$[1 - c_i(x)] f_c(x, t) + c_i(x) u_v(x, t), \quad (21)$$

where  $\Delta x_{ia}$  is approximately one TS wave-length, to guarantee a smooth transition to the domain further downstream where instantaneous  $u_v$  values are applied. Sudden changes of  $x_{ia}(t)$  at the step from one TS-period to the next are avoided by a smooth temporal adaption of  $c_i(x)$ .

Nevertheless, even very close to the inflow boundary the model originally induced comparably strong oscillations. The buffer domain at the free-stream boundary (section 2.2) proved necessary to keep these oscillations sufficiently low. During the breakdown of the laminar boundary layer, vortices are injected into the potential flow. Without the buffer domain, the wall-normal velocity component related to these vortices would be interpreted as rapidly changing boundary-layer thickness, if they touch the free-stream boundary.

If the disturbances are periodic with respect to the TS-frequency, the mean does not vary from one TS-period to the next. In the region with polynomial function ( $x < x_{ia}$ ) periodic flow is assumed by approximating the mean. If the DNS finally gains the desired periodic state, this assumption introduces no additional simplifications into the numerical code but, in contrast, removes errors which are generated further downstream by the modeling of TS-waves and vortices with large amplitude even far out in the potential flow.

The computation time for the interaction model is below 1% of the CPU-time of the whole numerical scheme.

### 3 Numerical test case

In an experiment in the laminar flow wind tunnel of our institute, the natural transition in a laminar separation bubble on a wing section with a chord-length of  $\hat{c} = 0.615 \text{ m}$  was investigated [23]. The free-stream velocity  $\hat{u}_\infty$  is  $29.3 \frac{\text{m}}{\text{s}}$ . Accordingly, the chord Reynolds number is  $Re_c = 1.2 \times 10^6$ . In the DNS the reference length is chosen to be  $\hat{L} = 0.0615 \text{ m}$ . The non-dimensionalized streamwise location  $x = 10$  is equivalent to 100% chord and the resulting Reynolds number in DNS is  $Re = 1.2 \times 10^5$ .

In the experiments, two velocity distributions  $u_p(x)$  at the edge of the boundary layer have been measured. The first one (diamonds in figure 3) refers to a flow with a separation bubble. For the turbulent second one, the separation has been suppressed by fixing a turbulator upstream of laminar separation (circles). The difference between the two is due to displacement effects. The crosses mark the distribution which corresponds to the pressure at the wall in the case with separation bubble. To test the interaction model, the turbulent distribution was approximated by a polynomial function (figure 3, solid line) and prescribed as boundary condition  $u_p$  in the DNS. The range at the inflow boundary ( $5.0 < x < 6.0$ ), where the velocity is constant (Blasius flow), is not shown. If the interaction model works properly, the DNS should finally approximate the experimental conditions with separation bubble (diamonds).

#### 3.1 Variation of the height of the integration domain

Since the 3D part of the DNS code was unchanged, extensive 2D simulations were performed to test and validate the numerical model. In five simulations the height of the integration domain was varied between  $y_e = 7.29 \delta_{1,s}$  (1) and  $19.44 \delta_{1,s}$  (5). With a constant grid spacing ( $\Delta y = 0.31$ ) this corresponds to 145 (1) and 385 grid points (5) in wall-normal direction, respectively. In streamwise direction the grid has 690 points. A TS wave-length is discretized with approximately 40 grid points. In each case the same free-stream velocity distribution  $u_p$  was prescribed, and a 2D TS-wave with an amplitude of  $U_{TS} \equiv 10^{-4}$  was forced at the disturbance strip far upstream of the LSB ( $5.21 < x < 5.52$ ).

For the investigation of transition mechanisms, the quality of DNS results mainly depends on an accurate reproduction of the disturbance development. Thus, the independency of the DNS results from the height of the integration domain is evaluated by comparing the amplitude profiles of the forced TS-wave  $U_{TS}$  and its first higher harmonic  $U_2$  at three streamwise locations in the different integration domains (figure 4). To examine the influence of displacement effects on the boundary layer, the mean profiles  $\bar{u}$  at the respective positions are also included. At the onset of the adverse pressure gradient, location (a), the mean-flow profile has almost Blasius shape and the TS-amplitude of 0.025% is in the linear regime. Consequently, the higher harmonic is negligible (except for the lowest domain (1), solid line).

At station (b) the reverse mean-flow velocity near the wall indicates the

separation bubble. The potential flow begins at  $y/\delta_{1,s} \approx 3.2$ . It is significantly accelerated compared to the prescribed potential velocity at this  $x$ -position, which is included as a vertical line. The deviation declines with increasing wall distance. The TS-wave is already strongly non-linear and a higher harmonic with large amplitude is present. At the upper boundary of domain (1) the TS-wave has an amplitude of almost 1%. Nevertheless, the profile of simulation (1), solid line, fits well with the other simulations. Obviously, the interaction model derives a very accurate boundary condition for TS-waves. Behind the bubble (position c), the potential flow is decelerated. The mean-flow profile has an almost turbulent shape due to the saturated TS-amplitude. The amplitude and wall-normal extent of the higher harmonic is significantly increased once more. The model predicts correct boundary conditions for disturbance waves even if disturbances with different frequencies and non-linear amplitude are present at the free-stream boundary (in domain (1):  $U_{TS}(y_e) \approx 4\%$ ,  $U_2(y_e) \approx 1\%$ ). In the three highest domains (3), (4), (5) the number of sources in the interaction model was limited to  $I = 74$ : each TS-wave length is modeled with only five sources, a wave length of the first higher harmonic covers less than three sources. In the simulations (1) and (2) it is twice that number.

To study the limits of the region where the application of the model is justified, a more detailed investigation of the slight differences between the computations is necessary. Position (a) is in the region where the temporal behavior at the free-stream boundary is approximated by a polynomial function ( $x < x_{ia}$ ) and hence does not allow for oscillations. The fundamental profile  $U_{TS}$  in computation (1), solid line, differs from all other simulations, which, in contrast, fit well to each other. The difference is the largest near the free-stream boundary of integration domain (1). In the simulations (2) - (5) the fundamental wave  $U_{TS}$  has a significant amplitude at the wall-normal distance of the free-stream boundary of domain (1). In simulation (1) oscillations with fundamental frequency are suppressed, whereas a slow drift is prescribed through the polynomial function. Thus, the amplitude in simulation (1) at the free-stream boundary represents the Fourier transform of this drift and is not due to a harmonic oscillation. Thereby, the distribution in a wide range towards the wall is affected including the second maximum of the TS-wave at  $y \approx 1.9 y/\delta_{1,s}$ . Additionally, a higher harmonic  $U_2$  is generated. Prescribing the analytical function, thus may impair the identification of TS-waves. It should be noted, however, that the disturbance amplitude  $U_{TS} \approx 2.5 \times 10^{-4}$  at location (a) is very small and that the near-wall maximum agrees well in all computations. Moreover, the further disturbance development is not affected (positions (b) and (c)).

The disturbance amplitude in simulation (5), dotted lines, at position (a) and (b) at the near-wall maximum of the TS-wave is approximately 8% larger than in the other computations. Especially at station (b), the whole profiles computed in domain (5) differ slightly from the other simulations. A close-up view on the velocity distribution in the potential flow at a constant distance from the wall (figure 5) shows the reason. In case (5), dotted line, the onset of the strong deceleration and the related higher TS-amplification

takes place a little further upstream than in the other cases. Apart from this, the distributions are quite similar. Namely, the process of disturbance growth and disturbance saturation evolves slightly upstream in comparison with the other cases. The saturated state apparently almost freezes any further disturbance development, since the breakdown into fine-scale turbulence is suppressed due to the lack of three-dimensionality. Therefore, when the saturated state is once attained in all computations, differences almost disappear (location c). If three-dimensionality is considered, there would be direct impact on the onset of transition to turbulence and consequently the entire re-attachment region. Simulation (5) thus marks the upper limit, where the assumptions in the model are justified. On the contrary, domain (1) represents the lower limit since it covers just one boundary-layer thickness at the outflow boundary. In between, the results are independent of the height of the integration domain.

## 3.2 Variation of forcing amplitude

In the underlying experiments neither the exact initial amplitude of the TS-waves nor their frequency distribution and spanwise wavenumber spectrum could be determined, because the TS-amplitude was far below the resolution properties of the hot-wire probe and signal-processing used. Before the interaction model was available, the separation bubble in DNS was much shorter than the one observed in the experiments. This was regarded to be due to different initial conditions of the TS-waves, especially different initial amplitudes. Therefore, 2D test calculations were performed aiming at the reproduction of the experimental findings by a variation of the forced initial disturbance amplitude in DNS. However, this attempt failed. The maximum shape parameter  $H_{12,max} = 6.75$  agrees well with the experiment (figure 6, symbols) if a TS-wave with an initial amplitude of  $U_{TS} \equiv 10^{-4}$  is forced (case **w4**, long dash-dotted line). The location of the onset of transition and re-attachment, indicated by the decay of the shape parameter, is in case **w4** far upstream compared to the experiment. If the initial amplitude is lowered to  $U_{TS} \equiv 10^{-5}$  (case **w5**, short dash-dotted line) the maximum grows strongly to  $H_{12,max} = 8.75$  but still the bubble remains further upstream. This result indicates an increased height and reverse-flow intensity in the separation bubble.

### 3.2.1 Influence of boundary-layer interaction

With the interaction model applied, in contrast, a reduction of the TS-amplitude from  $10^{-4}$  (case **w4ia**, long dashes), to  $10^{-5}$  (case **w5ia**, short dashes), and finally  $10^{-6}$  (case **w6ia**, dots) delays re-attachment, and the experimental distribution in the separated region is approximated much better in cases **w5ia** and **w6ia**. Downstream of the bubble, the experimental results indicate turbulence ( $H_{12} \approx 1.5$ ) whereas the DNS values are significantly higher due to the two-dimensionality. In cases with the same initial TS-amplitude the shape-parameter maximum is lower if the boundary-layer

interaction is considered. This elucidates the damping influence of displacement effects on the size of the separation bubble.

The time averaged streamwise velocity fields in the vicinity of the separation bubble without and with interaction model (**w5** and **w5ia**) are plotted in figure 7a) and b), respectively. The isolines  $\bar{u} = 0$  are emphasized. Additionally, in figure 7b) the  $\bar{u} = 0$  isoline of case **w5** is included to enable a direct comparison of size and shape of the separation bubble in both cases. The wall-normal direction is stretched by a factor of 20 in comparison with the  $x$ -coordinate. As seen above, the restrictive boundary condition with neglected interaction effects, fixes the separation bubble in streamwise direction. Thus, the flow separates further upstream and the angle of the isoline  $\bar{u} = 0$  at separation is larger. The separation bubble is taller. The reverse-flow velocity maximum is 21 %  $u_\infty$  in this case and 19 %  $u_\infty$  in case **w5ia**. The shape parameter is maximum at the positions  $x \approx 7.55$  (**w5**) and  $x \approx 7.75$  (**w5ia**) in the two cases, which agree with those streamwise positions where the  $\bar{u} > 0$  isolines have the biggest distance from the wall, but are different from the streamwise positions with the reverse-flow maximum.

The curvature of the isolines in the shear layer in the upstream part of the separation bubbles tends to zero if the interaction model is applied (figure 7b). Without the model, the curvature is stronger ( $x = 6.75 - 7.5$ ). A comparison of the wall-pressure  $p_w$  helps to explain this phenomenon. All cases show the same characteristic properties (figure 8). In the region upstream of separation and in the front part of the separation bubble ( $x < 7.5$ ), the pressure is increasing until a strong negative peak is observed, which indicates a counter-rotating vortex in the bubble (figure 8a). Furthermore, the bubble is the tallest at approximately this location. Then, a sudden strong pressure increase occurs, indicating the diminishing height of the bubble and the strong convex curvature of the  $\bar{u}$  isolines in the re-attachment region. With interaction model, the reduction of the forcing amplitude mainly influences the location, where these characteristic properties of the pressure distribution are observed. The pressure increase in the separation region is shifted upstream in the case **w6ia**, dots in figure 8a, compared to cases **w5ia** and **w4ia**, short and long dashes, whereas the negative peak and the sudden pressure increase towards still growing final values is delayed (figure 8b). Without interaction model, the position of the bubble is almost fixed and the reduction of the forcing amplitude first of all causes changes of the pressure gradients. Upstream from separation ( $x < 7.0$ ), the pressure increases much stronger in the case **w5**, short-dash dotted, than in the case **w4**, long-dash dotted in figure 8a, forcing the convex  $\bar{u}$  isolines (figure 7a). In the front part of the bubble ( $7.0 < x < 7.5$ ), in contrast, the pressure increases only weakly in case **w5** and has the lowest value of all five cases, causing concave  $\bar{u}$  isolines. The end of the sudden pressure increase in the re-attachment region and the respective final pressure levels are almost similar in the cases **w4** and **w5** (figure 8b).

The velocity distributions at the edge of the boundary layer in all simulations contain a plateau due to the displacement of the separation bubble (figure 9). Without interaction model, the lowering of the disturbance ampli-

tude causes a strong growth of the height of the separation bubble, indicated by the high values of the shape parameter in case **w5**, that leads to an acceleration of the velocity in the plateau. Taking displacement effects into account (cases **ia**) the plateau is more distinct and the distributions with different amplitude compare well with each other until in the respective simulation the sudden deceleration begins which indicates re-attachment. The strong deceleration in the case with the lowest amplitude (**w6ia**) is at almost the same streamwise location as in the experiment. Upstream of the bubble, the edge velocity is decreased in comparison with the prescribed distribution  $u_p$  and separation thus takes place at a lower edge velocity than in the experiment. Subsequently, the edge velocity in the plateau in all DNS is slightly lower than in the experiment (diamonds). The DNS runs indicated by the index 3D will be explained further down.

### 3.2.2 Comparison with LST

In figure 10 the amplification curves of TS-waves for the cases **w4**, **w4ia**, **w5**, and **w5ia** are plotted for comparison with parallel linear stability theory (LST, dotted lines). Initially, they depend only on the forced amplitude. The early deceleration of the potential flow in the cases with interaction model (solid line) soon causes stronger disturbance amplification and at  $x \approx 6.0$  their amplitude becomes larger than in the computations without interaction model (dashed lines). At  $x \approx 6.8$  an inverse behaviour begins. The disturbance growth in the computations without interaction model becomes stronger and at  $x \approx 7.0$  their amplitude exceeds the amplitude of the respective run using the model. Finally, the amplitude saturates at almost the same streamwise locations despite their different initial amplitudes. In contrast, with the interaction model applied, wave saturation is delayed if the initial amplitude is decreased. For all cases the agreement between DNS and the parallel linear stability theory (LST) is very good, although it could be expected that at least in the separated region the non-parallel contributions to the stability properties might be too large to justify the assumption of parallel flow.

## 4 Transitional LSB

So far, all comparisons between DNS and experiment were more or less of qualitative nature, since turbulence was disabled in the DNS due to the lack of 3D disturbance modes. One would expect that no farther than  $x = 7.8$ , where the decay of the shape parameter in the experiment indicates the onset of transition, 3D modes play an important role and may no longer be neglected. Thus, the runs **w5ia** and **w6ia** were continued with a resolution of 44 spanwise spectral harmonics. These runs are marked by the index **3D**. After initial 3D perturbations were excited by pulse-wise forcing with very low amplitude, 3D modes start to grow in time (see Maucher *et al.* [9]) and finally transition to turbulence occurs. Actually, the respective edge-velocity distributions (thin lines in figure 9) deviate in the re-attachment region from

the 2D curves and the overshoot of the velocity distributions observed in the 2D cases upstream of the sudden decay vanishes. Case **w6ia<sub>3D</sub>** almost perfectly fits the experiment (diamonds).

Accordingly, the comparison of mean-flow profiles in this case **w6ia<sub>3D</sub>** with the experiment (symbols) shows very good agreement for all streamwise stations A–G (figure 11a). Initially, the flow is attached (position A). The shear layer then lifts from the wall (B) and the profiles exhibit an inflection point. At station (C) separation already took place and a tall reverse-flow region forms (D, E). Finally, a rapid disintegration of the shear layer occurs within only one TS-wavelength  $\lambda_{TS} \approx 0.3$  (F, G). All profiles agree well with the experiment. The differences at the positions F and G near the wall are probably due to the difficulties of the hot wire to resolve low mean velocities if the rms-amplitude is high. Moreover, at least at position F, the DNS gives evidence for the presence of reverse flow, which cannot be detected by the hot-wires either. This also causes the underestimation of the shape parameter in the experiment. The shape parameter maximum in the experiment, in fact, is expected to be larger and to agree better with case **w6ia** than indicated by figure 6.

Figure 11b shows a cut through the instantaneous spanwise vorticity  $\omega_z$  in the vicinity of re-attachment along the centerline of the airfoil at two time-instances separated by one half TS forcing period  $T_{TS}$ . The flow field is highly unsteady and a interpretation of the mean flow is misleading. In particular, no continuous breakdown of the free-shear layer and fine-scale turbulence spreading towards the wall and into the potential flow causing re-attachment is observed. In contrast, a periodic roll-up of the free shear layer occurs ( $t = t_0, x = 8.05$ ). The resulting large-scale vortex starts to propagate downstream and breaks down into fine-scale turbulence ( $t = t_0 + 0.5T_{TS}, x = 8.15$ ). Contributions to the understanding of transition or re-attachment cannot be expected from the investigation of the time-averaged flow field. Although the turbulence downstream of the separation bubble (re-attachment of the mean flow at  $x = 8.15$ ) is not yet fully resolved and there DNS results are only of qualitative nature, grid-refinement studies proved, that the re-attachment region is well-resolved and the discretization fulfills the requirements to quantitatively investigate the late non-linear stages of the transition mechanisms involved.

## 5 Conclusions

Despite big advances in DNS of laminar separation bubbles in the recent twenty years, 3D DNS at large Reynolds numbers as present on high-lift devices or laminar-flow airfoils are just at the very beginning. A major problem is to evaluate a free-stream boundary condition, if the viscous-inviscid boundary-layer interaction is not negligible. Here, the boundary-layer assumptions are violated, namely the wall-normal pressure gradient deviates from zero. Consequently, a measured pressure distribution (and the respective velocity distribution) at the wall or at the edge of the boundary layer

cannot be applied as free-stream boundary condition in DNS. Although it is possible to determine the correct distribution iteratively by doing a DNS, comparing the computed pressure distribution with the experiment, correcting the boundary condition, doing the next DNS and so on, this needs tremendous numerical effort and time. Additionally, such DNS depend on reliable measurements with exactly that conditions required in the physical problem subject of the investigation (initial disturbances, velocity distribution, etc).

In contrast, if an accurate boundary-layer interaction model is applied, DNS can be performed independently from experiments. Only a potential velocity distribution is needed, either calculated with a steady, inviscid numerical scheme or measured in experiments with separation suppressed by a turbulator (thus avoiding strong viscous-inviscid interaction). Comparisons with the experiment are much easier and more essential, since the results are not fitted from the beginning by comparisons but DNS and experiment are independent approaches to the same physical problem. DNS of the self-excited transition often suffer from unknown initial conditions (amplitude and character of disturbances in the boundary layer). Without interaction-model, agreement with experiments can be strived for by varying the initial conditions *or* by adapting the free-stream velocity distribution. With a model, only the influence of the initial disturbance amplitude has to be taken into account.

The application of the interaction model renders fundamental numerical experiments on basic mechanisms in laminar separation bubbles possible without the necessity of continuous comparisons with measurements. In DNS, the initial conditions can be fixed much easier and more accurate than in experiments, which is needed for investigations of interactions of different 2D and 3D disturbance waves with low initial amplitude. Thus, DNS can be expected to make large contributions to the understanding of the physics of laminar separation bubbles.

Finally, an interaction model is able to catch displacement effects of high-frequency disturbances in the boundary layer and to compute the respective instantaneous boundary condition. Consequently, DNS with interaction model applied require a lower integration domain than without model, saving a remarkable amount of memory and computation time.

**Acknowledgments:** The authors would like to thank F. R. Hama for the proof reading and his useful comments. The financial support of the Deutsche Forschungsgemeinschaft (DFG) for the financial support under grant Ri 680/1 is gratefully acknowledged.

## References

- [1] Gruber K., Bestek H., and Fasel H., "Interaction between a Tollmien-Schlichting wave and a laminar separation bubble", AIAA 87-1256, 1987.
- [2] Gruber K., "Numerische Untersuchungen zum Problem der Grenzschichtablösung", Dissertation, Universität Stuttgart, *Fortschritt-Berichte VDI Reihe 7*. VDI-Verlag, Düsseldorf, 1988.

- [3] Pauley L. L., Moin P., and Reynolds W. C., “The structure of two-dimensional separation”, *J. Fluid Mech.*, Vol. 220, 1990, pp. 397–411.
- [4] Lin J. C. M. and Pauley L. L., “Unsteady Laminar Separation on Low-Reynolds-Number Airfoils”, AIAA 93-0209, 1993.
- [5] Ripley M. D. and Pauley L. L., “The unsteady structure of two-dimensional steady laminar separation”, *Phys. Fluids A*, Vol. 5, No. 12, 1990, pp. 3099–3106.
- [6] Rist U., “Nonlinear effects of 2D and 3D disturbances on laminar separation bubbles”, *Proc. IUTAM-Symposium on Nonlinear Instability of Nonparallel flows*, edited by S.P. Lin, Springer, New York, 1994, pp. 324–333.
- [7] Rist U. and Maucher U., “Direct Numerical Simulation of 2-D and 3-D Instability Waves in a Laminar Separation Bubble”, *Application of Direct and Large Eddy Simulation of Transition and Turbulence, AGARD-CP-551*, 1994, pp. 34–1–34–7.
- [8] Rist U., Maucher U., and Wagner S., “Direct numerical simulation of some fundamental problems related to transition in laminar separation bubbles”, *Computational Methods in Applied Sciences '96*, edited by Désidéri *et al.*, John Wiley & Sons Ltd, 1996, pp. 319–325.
- [9] Maucher U., Rist U., and Wagner S., “Secondary instabilities in a laminar separation bubble”, *New Results in Numerical and Experimental Fluid Mechanics*, edited by H. Körner and R. Hilbig, Vol. 60 of *NNFM*, Vieweg, 1997, pp. 229–236.
- [10] Maucher U., Rist U., and Wagner S., “Transitional structures in a laminar separation bubble”, to appear in Proc. STAB Symposium, Berlin, 1998, *NNFM*. Vieweg, 1999.
- [11] Wasistho B., *Spatial Direct Numerical Simulation of Compressible Boundary Layer Flow*, Proefschrift (dissertation), Universiteit Twente, 1997.
- [12] Alam M. and Sandham N. D., Numerical study of separation bubbles with turbulent reattachment followed by a boundary layer relaxation, *Parallel Computational Fluid Dynamics*, edited by D. R. Emerson *et al.*. Elsevier Science B. V., 1998.
- [13] Spalart P. R. and Strelets M. K., Direct and reynolds-averaged numerical simulations of a transitional separation bubble, 11th Symposium on Turbulent Shear Flows, Grenoble, France (private communication, unpublished), 1997.
- [14] Alam M. and Sandham N. D., Direct numerical simulation of ‘short’ laminar separation bubbles with turbulent reattachment, submitted to *J. Fluid Mech.* in October 1998.

- [15] Wasistho B., Geurts B. J., and Kuerten J. G. M., “Numerical simulation of separated boundary-layer flow”, *Journal of Engineering Mathematics*, Vol. 32, 1997, pp. 177–194.
- [16] Hsiao C.-T. and Pauley L. L., “Comparison of the triple-deck theory, interactive boundary layer method, and Navier-Stokes computation for marginal separation”, *Transactions of the ASME*, Vol. 116, 1994, pp. 22–28.
- [17] Hildings C., Simulation of laminar and transitional separation bubbles, Technical report, Royal Institute of Technology, Stockholm, Sweden, 1997, PhD thesis.
- [18] Schlichting H. and Truckenbrodt E., “Aerodynamik des Flugzeugs.”, Springer, 1st edition, 1959.
- [19] Veldman A. E. P., “New, quasi-simultaneous method to calculate interacting boundary layers”, *AIAA J.*, Vol. 19, No. 1, 1981, pp. 79–85.
- [20] Rist U. and Fasel H., “Direct numerical simulation of controlled transition in a flat-plate boundary layer”, *J. Fluid Mech.*, Vol. 298, 1995, pp. 211–248.
- [21] Kloker M., Konzelmann U., and Fasel H., “Outflow boundary conditions for spatial Navier-Stokes simulations of transitional boundary layers”, *AIAA J.*, Vol. 31, No. 4, 1993, pp. 620–628.
- [22] Fasel H., Rist U., and Konzelmann U., “Numerical investigation of the three-dimensional development in boundary layer transition”, *AIAA J.*, Vol. 28, No. 1, 1990, pp. 29–37.
- [23] Würz W. and Wagner S., “Experimental investigations of transition development in attached boundary layers and laminar separation bubbles”, *New Results in Numerical and Experimental Fluid Mechanics*, edited by H. Körner and R. Hilbig, Vol. 60 of *NNFM*, Vieweg, 1997, pp. 413–420.

# List of Figures

1	Integration domain. . . . .	23
2	Interaction model: a) qualitative streamwise distribution of the mean $\bar{u}_v(x)$ (dashed) and amplitude $U_v(x)$ (solid line) of the induced velocity in a TS-period. b) temporal approximation of the mean $\bar{u}_v$ (circles) upstream of the LSB $x < x_{ia}$ , if $\bar{u}_v$ is time-independent; error bars show required accuracy $\pm \varepsilon_{inst}$ . c) damping of variations of $\bar{u}_v$ with the amplitude $A_{mean}$ (circles) upstream of the LSB $x < x_{ia}$ : $A_{mean} = \varepsilon_{inst}$ (solid line), $A_{mean} = 0.5\varepsilon_{inst}$ (dashed line) and $A_{mean} = 0.1\varepsilon_{inst}$ (dash-dotted line). . . . .	23
3	Velocity distributions in the experiment (symbols) and boundary condition for the DNS (line). $x = 10 \equiv 100\%$ chord length.	24
4	Comparison of the mean-flow $\bar{u}$ , the TS-wave $U_{TS}$ , and its first higher harmonic $U_2$ at a) $x = 6.5$ , b) $x = 7.7$ , and c) $x = 8.0$ in 5 integration domains with varying height (1) – (5). . . . .	24
5	Comparison of the streamwise velocity component at $y = 3.24 \delta_{1,s}$ in the computations (1) - (5). . . . .	25
6	Comparison of the shape parameter from the experiment (symbols) and the DNS. . . . .	25
7	Isolines of time averaged streamwise velocity component $\bar{u}$ without and with the interaction model in case <b>w5</b> a) and <b>w5ia</b> b), respectively. Lines $\bar{u} = 0$ highlighted. $\bar{u} = -0.2, -0.15, \dots, 1.0$ and $-0.04, -0.03, -0.02, -0.01$ . Negative values dashed.	26
8	Wall-pressure distributions: a) up to the re-attachment and b) including the region downstream of the bubble. . . . .	27
9	Comparison of the velocity distributions in the experiment (symbols) and in the DNS. . . . .	27
10	Amplification of the forced TS-wave with the frequency $\beta = 10$ : comparison of DNS (solid line with interaction model, dashed line without) with linear stability theory (dotted). $x = 10 \equiv 100\%$ chord length. . . . .	28
11	Case <b>w6ia<sub>3D</sub></b> : a) mean-flow profiles at different streamwise stations in comparison with the experiment (symbols), b) spanwise vorticity $\omega_z$ along the centerline ( $z = 0$ ) in the vicinity of re-attachment at two time-instances separated by one half forcing period $T_{TS}$ . . . . .	28

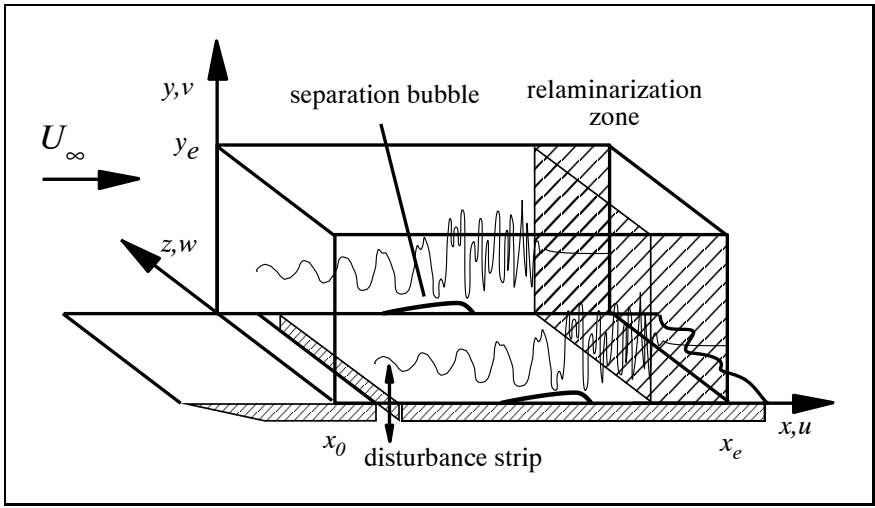


Figure 1: Maucher, Rist, Wagner

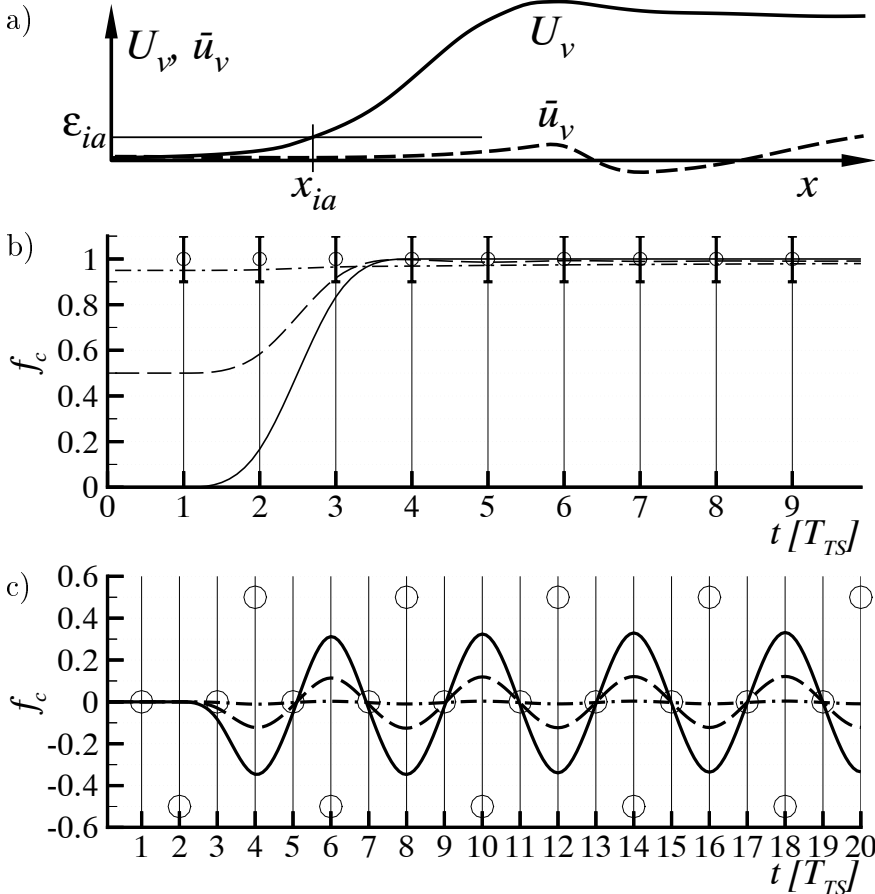


Figure 2: Maucher, Rist, Wagner

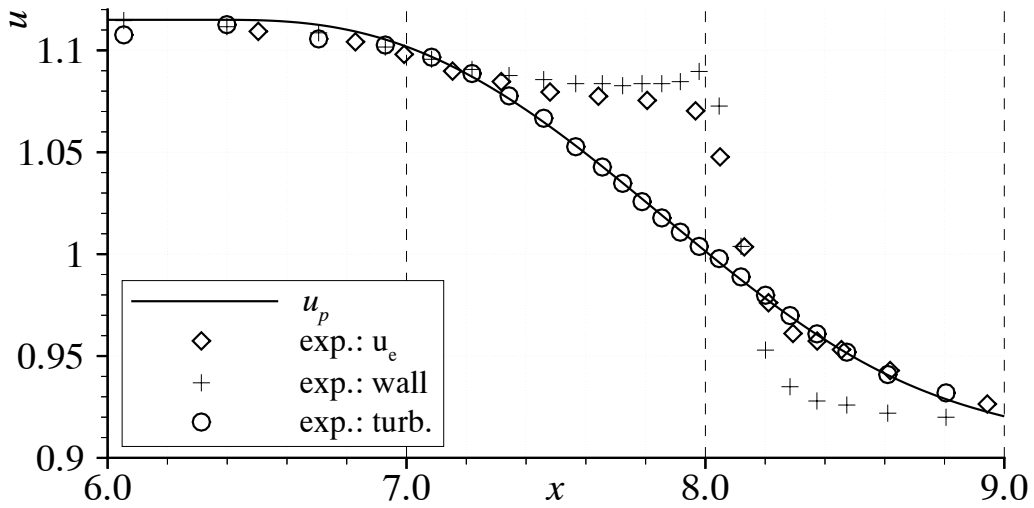


Figure 3: Maucher, Rist, Wagner

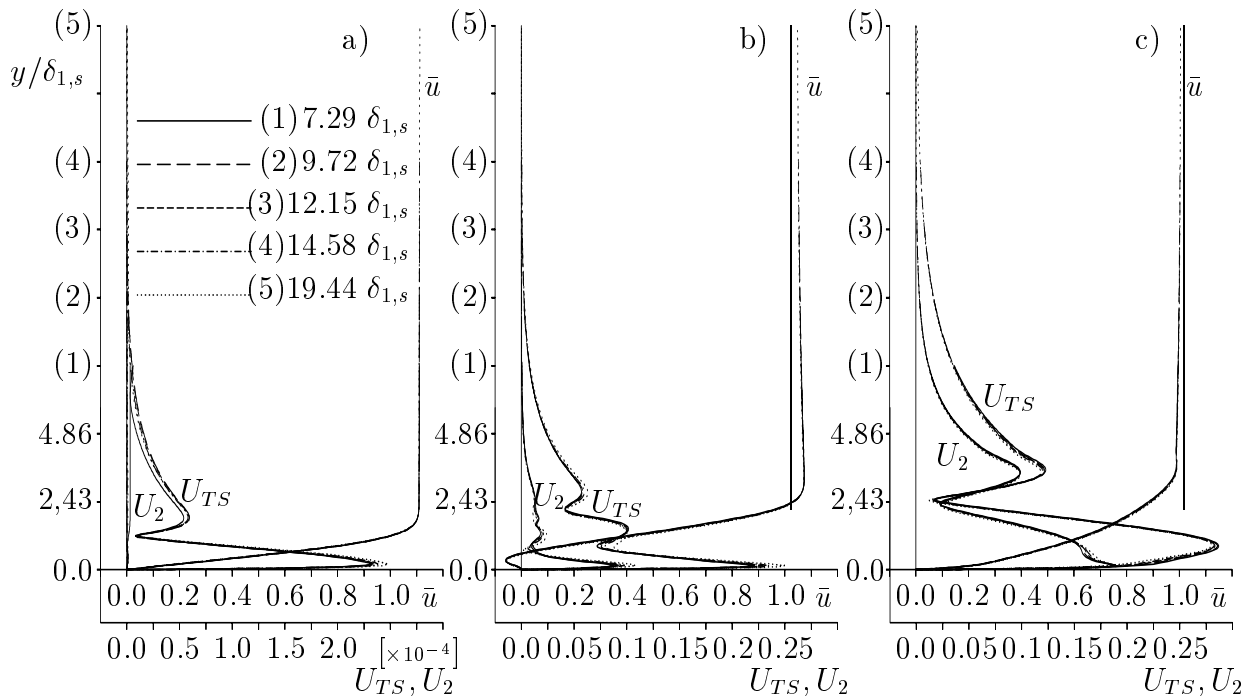


Figure 4: Maucher, Rist, Wagner

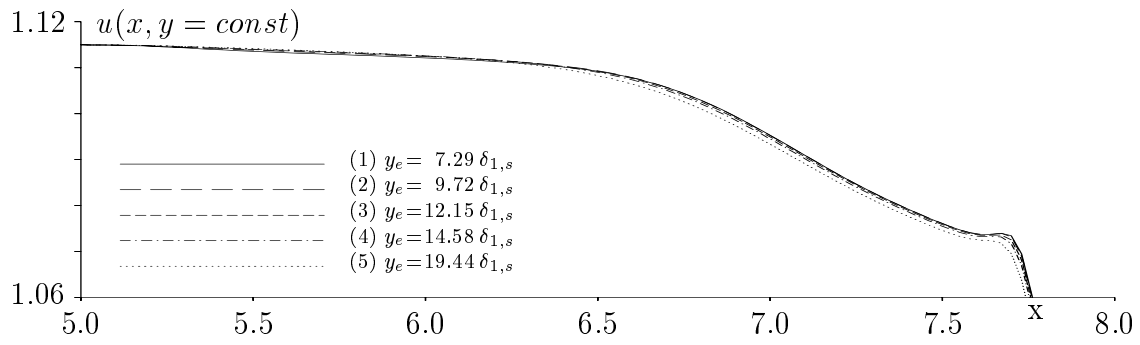


Figure 5: Maucher, Rist, Wagner

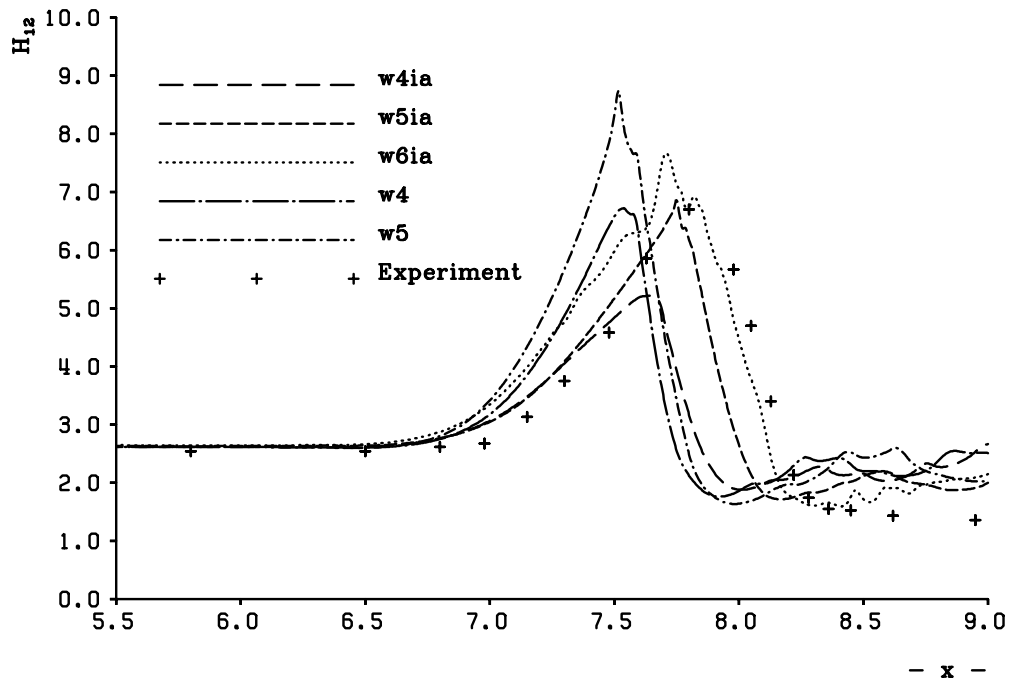


Figure 6: Maucher, Rist, Wagner

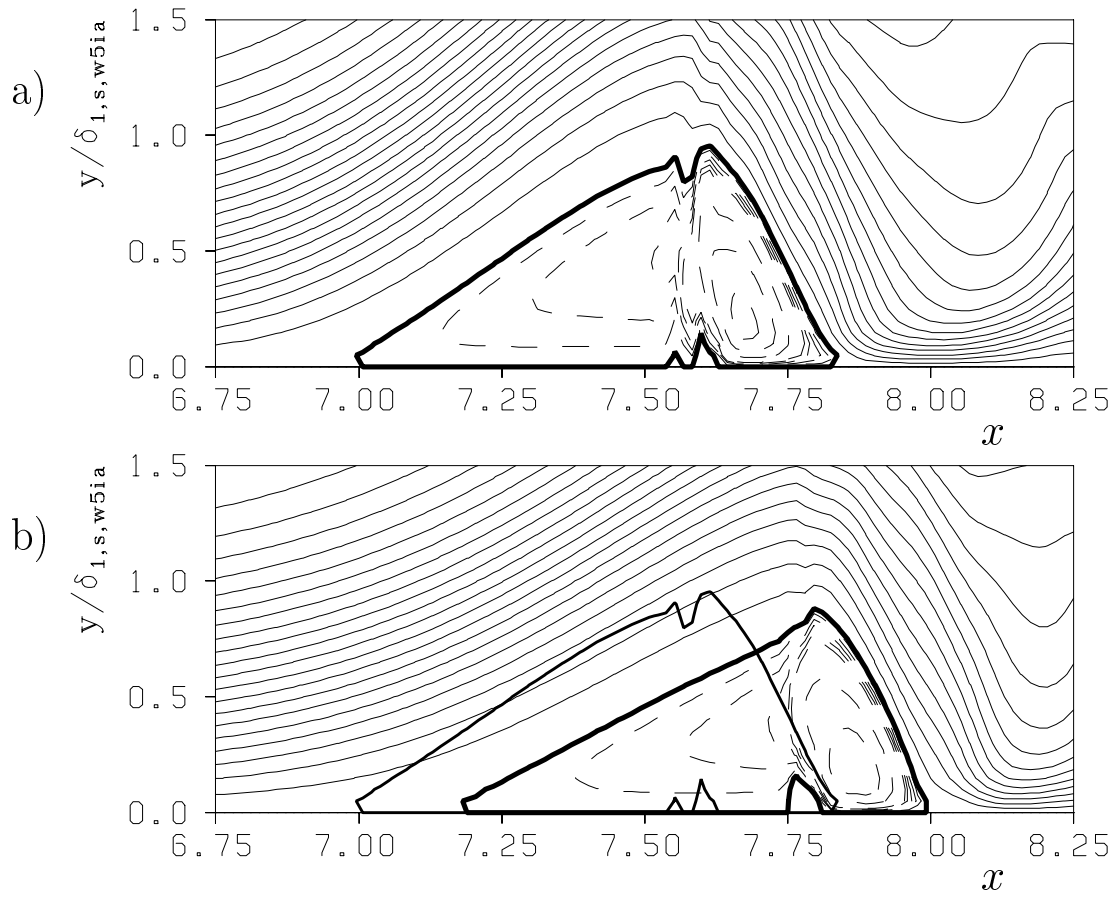


Figure 7: Maucher, Rist, Wagner

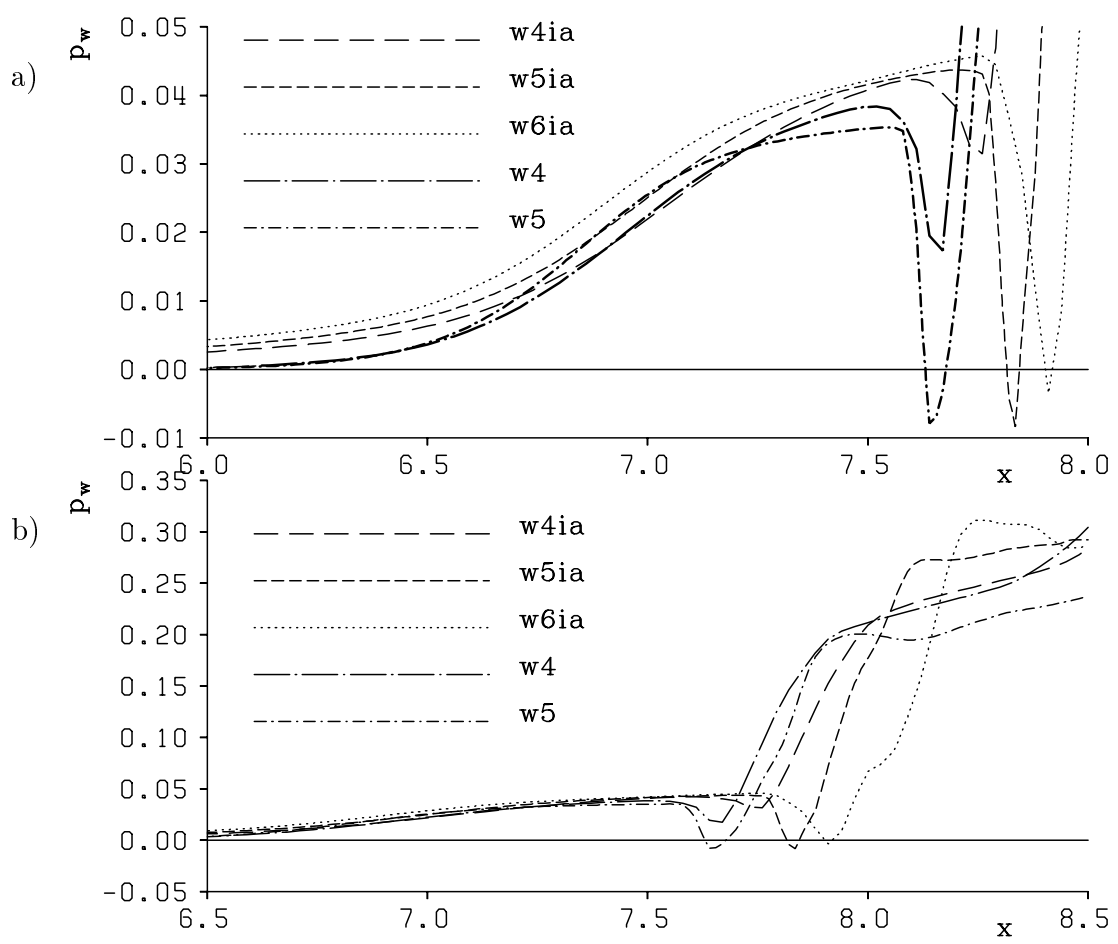


Figure 8: Maucher, Rist, Wagner

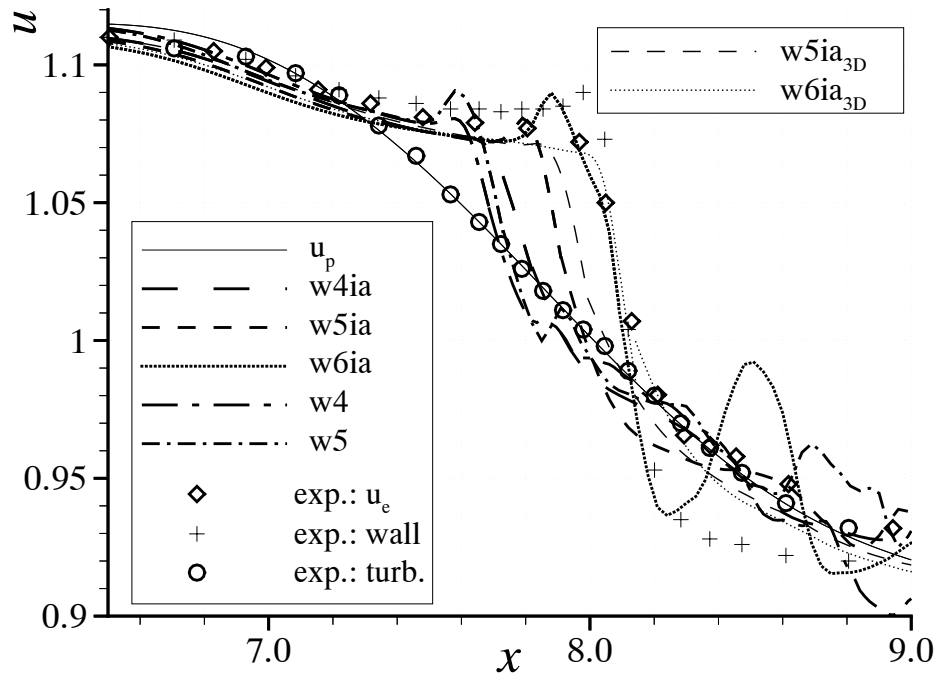


Figure 9: Maucher, Rist, Wagner

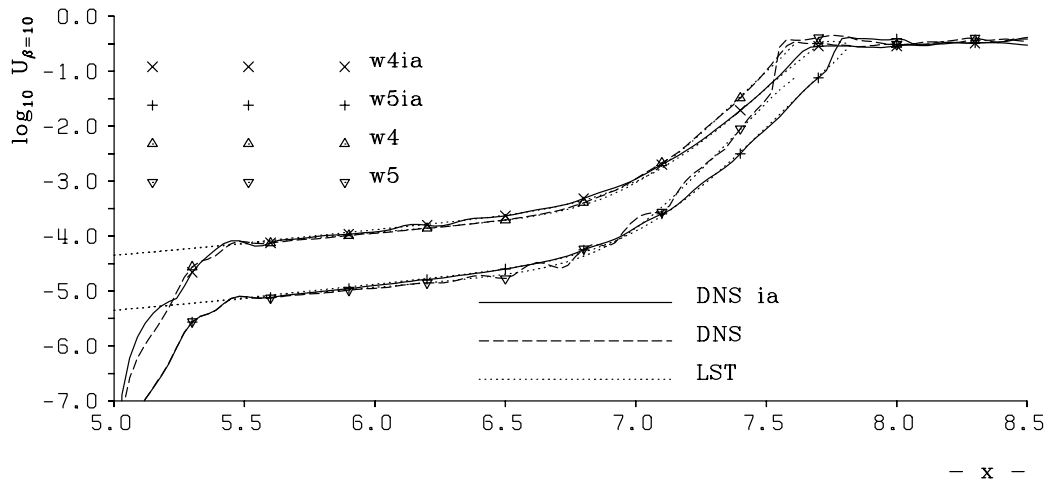


Figure 10: Maucher, Rist, Wagner

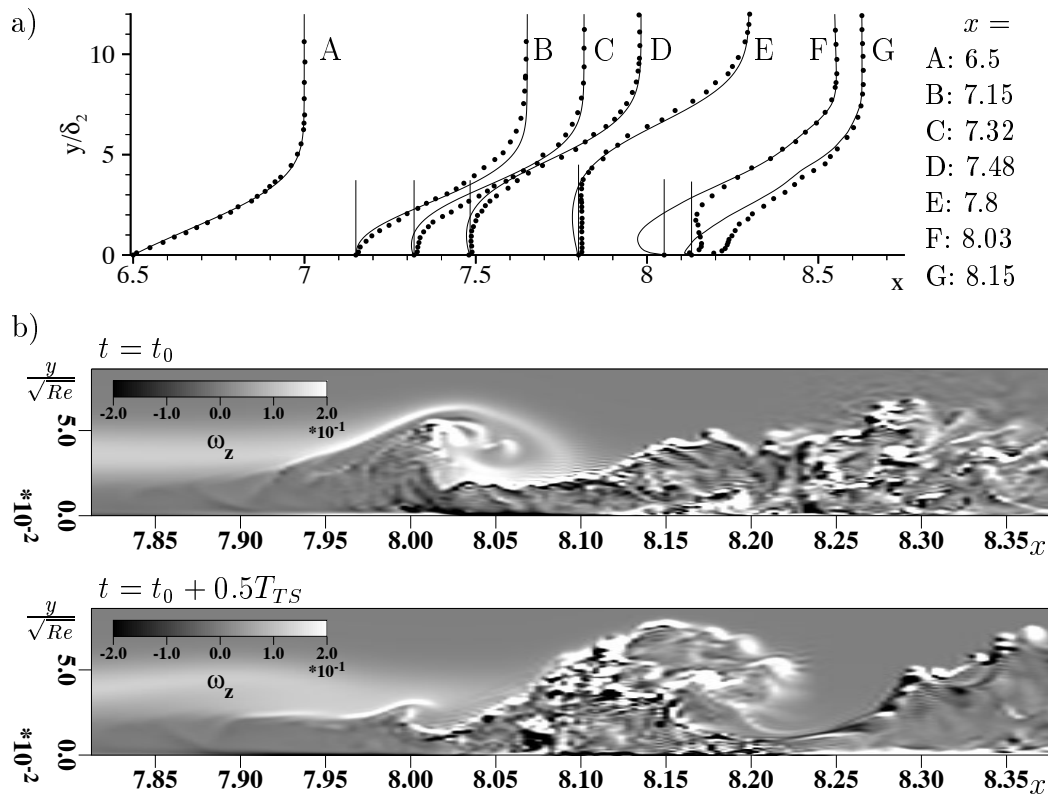


Figure 11: Maucher, Rist, Wagner